





Numerical and experimental investigation on a conical poppet relief valve with flow force compensation

Roberto Finesso  and Massimo Rundo 

Dipartimento Energia, Politecnico di Torino, Torino, Italy

ABSTRACT

Numerical and experimental investigations have been carried out in order to study the effect of the poppet geometry on the flow-pressure characteristic of a direct acting pressure relief valve, which is equipped with a flow deflector for flow force compensation. A dynamic 3D-CFD model was built in ANSYS Fluent™, which is capable of simulating the interaction between the fluid flow and the poppet dynamics by means of mesh deformation and of a user-defined function (UDF). This model was applied to predict the flow-pressure characteristics of the valve for different spring preload settings and deflector geometries. The simulated curves were validated using experimental data acquired at FPRL (Fluid Power Research Laboratory) at the Politecnico di Torino, and an excellent agreement was found. The CFD model was then used to predict the effect of geometric parameters of the poppet, such as the cone angle and the position of the deflector. Finally, a 0D model has been developed in order to predict the flow forces; this model requires very few calibration points using 3D-CFD simulations, and can easily be implemented in lumped parameter simulation tools. It was found that this model leads to a satisfactory prediction of the flow-pressure characteristic of the valve.

ARTICLE HISTORY

Received 16 September 2015
Accepted 15 February 2017

KEYWORDS

Relief valve; conical poppet;
flow forces; CFD

1. Introduction

Direct acting poppet-type pressure relief valves are extensively adopted in fluid power systems, as they are low-cost, dirt tolerant and robust components. The achievement of an optimal flow-pressure characteristic for this type of valve requires an effective compensation of the effect of the flow forces acting on the poppet and of the spring stiffness, which is usually high.

Among the different solutions proposed in the past years, the adoption of a flow deflector integral with the poppet (Domagala and Lisowski 2003, 2004) or of a rim in the rear part of the poppet (Vaughan *et al.* 1991, 1992, Andersen *et al.* 2003) has proved to be an effective solution to achieve an optimal valve characteristic. This solution in fact allows the jet outflowing from the metering edge to be deflected, so as to generate an opening force that may balance both the flow force which tends to close the poppet and the incremental closing force due to the high spring stiffness.

The optimization of the geometry of the flow deflector is of great importance in order to obtain an optimal valve characteristic for different operating conditions. This optimization can be carried out either experimentally or numerically. The experimental approach would require the manufacturing of different poppet geometry

configurations and their characterization on a test rig; numerical optimization is based, instead, on the generation of several virtual models of the valve by means of a Computer Aided Design (CAD) software, and on the simulation of the fluid flow inside the valve, as well as of the flow forces, by means of 3D-CFD codes.

The main advantage of the numerical optimization approach is related to the saving of the costs related to the manufacturing of the prototypal poppet geometries; however, this method needs to be validated over several operating conditions, in order to guarantee its self-consistency and a satisfactory accuracy in the results. Several examples of 3D-CFD simulations of poppet valves can be found in the literature (Huguet 2003, 2004, Jalil *et al.* 2015). 3D-CFD simulations have proved to be a reliable and effective method to determine the flow forces, also for spool-type valves (Del Vescovo and Lippolis, 2003).

The main focus of the present research is the development, in ANSYS Fluent™, of a dynamic 3D-CFD model of a direct-acting poppet-type pressure relief valve, and the evaluation of the effect of the geometry of the flow deflector and of the poppet on the flow-pressure characteristic. The developed approach is capable of simulating the interaction between the fluid flow inside the valve and the poppet dynamics, by means of the use of

a dynamic mesh and of a user-defined function (UDF). The UDF is used to update the position of the poppet at each time instant, on the basis of the evaluation of the forces acting on the poppet itself, including the contributions of the spring and of the fluid; the latter contribution is evaluated taking into account the pressure field information that derives from the CFD solution. The CFD mesh is then deformed at the new time instant, on the basis of the new position of the poppet that is evaluated by the UDF, and the flow and pressure field solutions are then solved by the CFD code. This method allows a direct simulation of the flow-pressure characteristic of the valve to be obtained, for a given spring preload. It is in fact sufficient to set the preload of the spring in the UDF, as well as the initial poppet opening position, and to set the inlet flow rate; the dynamic simulation is then run, and the inlet valve pressure can be evaluated at the end of the simulation when the poppet achieves the steady-state position. The flow-pressure characteristic can thus be derived point by point, by setting different inlet flow rates and different spring preloads. The CFD simulations were carried out using the cavitation model embedded in ANSYS Fluent, in order to avoid the occurrence of negative absolute pressure values (Gao *et al.* 2002, Bernad and Resiga 2012). An alternative approach to evaluate the flow-pressure characteristic of the valve is based on lumped-parameter modelling environments. These tools are based on analytical models to evaluate the forces acting on the poppet, but the force generated by the flow deflector is not included. A correct estimation of such contribution would require a large number of steady-state 3D-CFD simulations to be carried out (for different flow rate and poppet opening conditions), in order to build a look-up table of the force which can be implemented in the lumped-parameter modelling tool. This procedure is however time consuming. For this reason a customized 0D model has been developed and implemented in the LMS Imagine.Lab AmesimTM environment in order to evaluate the forces acting on the flow deflector. It will be shown that this model is characterized by a very simple tuning, as it requires only a few 3D-CFD simulations to be carried out.

2. Valve geometry and experimental setup

The valve used as reference unit for the present study is a conical poppet direct acting pressure relief valve shown in Figure 1. The valve is provided with a damper constituted by a cylinder connected through a rod to the conical poppet. The left end of the adjustable spring is in contact against the poppet through a washer, called flow deflector, which deviates the flow coming from the metering edge. The spring chamber is drained to the T port through a hole. In the figure the location of the pressure transducers used for sensing the inlet and outlet pressures in the experimental tests described hereinafter are also shown.

A detail of the valve cartridge in regulating conditions is reported in Figure 2. Since the diameters of the poppet seat and of the damper are the same, when the valve is closed, only the pressure acting of the right frontal surface of the damper generates the opening force F_{act} to oppose the spring force F_{spr} . In steady-state conditions such pressure coincides with the inlet pressure at the port P.

In regulating conditions two additional forces arise: the flow force F_{jet} due to the reduction of the pressure along the conical poppet just upstream the metering edge and the force F_{def} generated by the flow deflector.

Three different configurations of the flow deflector were tested experimentally. In particular, in addition to the baseline geometry referred to as ‘Geometry A’, a spacer of 0.5 mm (Geometry B) and of 1.0 mm (Geometry C) were added in order to investigate the effect of the deflector depth on the flow-pressure characteristic. The geometrical parameters of the valve are listed in Table 1.

The hydraulic scheme of the test rig is reported in Figure 3. The flow rate was generated by a 40 cc/rev variable displacement pump equipped with absolute pressure limiter, which was set to 100 bar. The pump was driven by a constant speed 15 kW electric motor. A two-port flow control valve RQ2 was used to impose the flow rate through the valve under test.

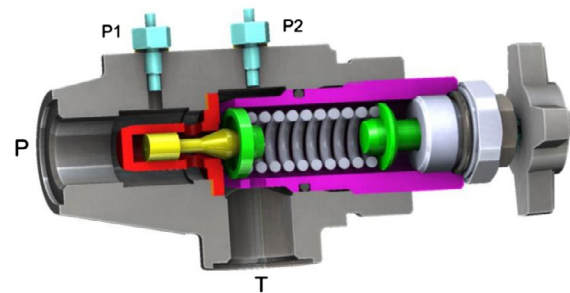


Figure 1. 3D section view of the valve.

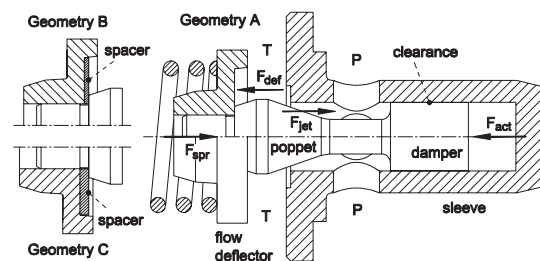


Figure 2. Detail of the cartridge.

Table 1. Main valve parameters.

Quantity	Value
Popped seat/damper diameters d_s	8 mm
Cone half angle α	19.2°
Deflector depth – baseline	1.5 mm
Spring stiffness	51 N/mm
Max cracking pressure	75 bar

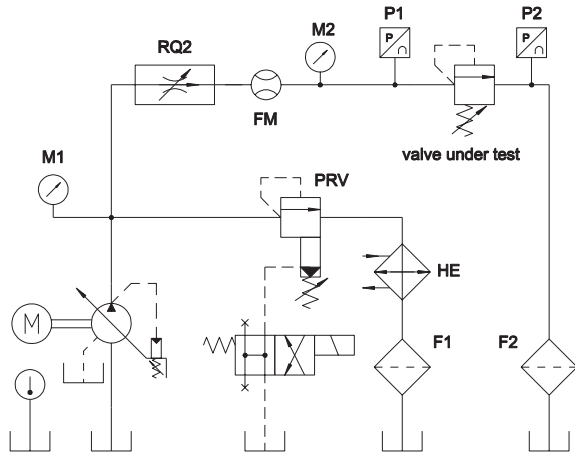


Figure 3. Hydraulic circuit according to ISO standard.

The flow rate was measured by a turbine flow meter KEM-KUPPERS HM11 E with 6–60 L/min measuring range. The pressure at the inlet of the valve under test was sensed by a miniature absolute pressure transducer (P1) GS XPM, with 0–100 barA range and $\pm 0.25\%$ linearity error. A similar transducer (P2) with 0–20 barA range was used to measure the pressure at the valve outlet. A water-oil heat exchanger was used to cool the fluid at the end of each test by venting the piloted relief valve PRV. The rig utilized an ISO VG 46 DTE25 oil stored in a 100 L reservoir. A view of the test rig along with the instrumentation is shown in Figure 4.

For each geometrical configuration, three flow-pressure characteristics were acquired at the test rig, by setting low (15 bar), medium (45 bar) and high (75 bar) spring preload settings.

3. Dynamic 3D-CFD model

3.1. Model description

A dynamic 3D-CFD model of the valve was realized by means of ANSYS Fluent, which is capable of simulating the interaction between the fluid flow and the poppet.

The realization of the CAD model of the valve, as well as the extraction of the fluid computational domain, were carried out in Solidworks™. The ANSYS meshing tool was then used to generate the finite-volume tetrahedral mesh; a positive poppet opening position was set as the initial geometric configuration, in order to avoid excessive mesh distortion with highly skewed cells during the initial poppet displacement. In particular, initial openings of 0.2, 0.5 and 1.0 mm were set for low ($Q \leq 10$ L/min), medium ($10 < Q < 30$ L/min) and high ($Q \geq 30$ L/min) flow rates, respectively, in order to speed up the achievement of the steady-state poppet position. A mesh refinement was realized in the metering edge zone, as well as in the fluid domain downstream from it, in order to capture accurately the jet deflection induced by the flow deflector, as well as the high velocity and pressure gradients. A refinement was also realized in

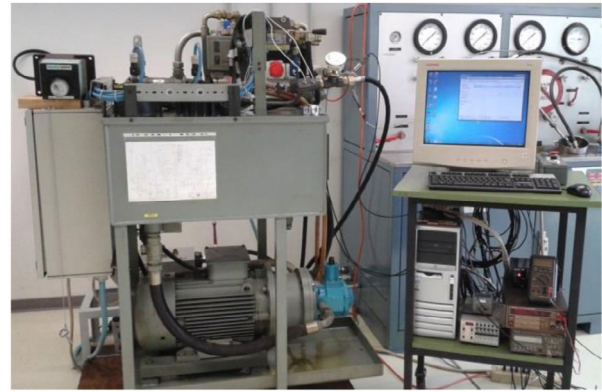


Figure 4. Photo of the test rig.

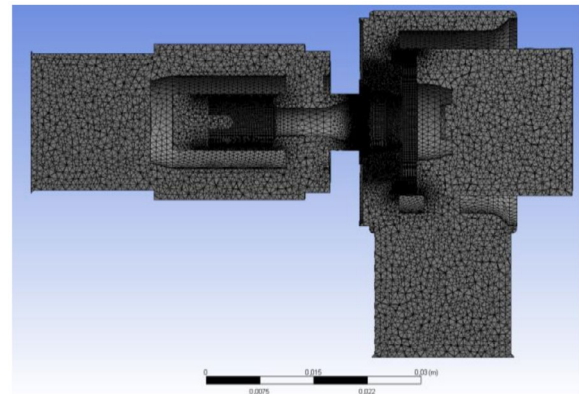


Figure 5. Final computational mesh for the baseline geometry.

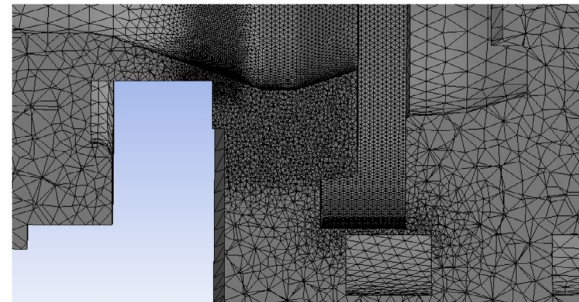


Figure 6. Detail in the metering edge and flow deflector zones.

the gap between the damper and the sleeve, as well as in the annular region around the flow deflector. A grid independence study was carried out in order to find the best trade-off between computational requirements and accuracy. The final computational mesh is shown in Figures 5 and 6, and includes a total number of about 2 million cells.

3.2. Model setup

3.2.1. Turbulence sub-model

A RANS approach has been adopted for the 3D-CFD analysis, using the standard formulation of the two

equation $k-\varepsilon$ model to resolve the Reynolds stress and close the equation set. The scalable wall-function approach was adopted instead of the standard wall-function one (ANSYS Fluent™ theory guide, 2011).

It is worthwhile recalling that the standard wall function approach is based on the Launder and Spalding results (Launder *et al.* 1974), according to which the boundary layer is divided into two sub-layers. The inner one is the viscous sub-layer ($y^* < 11.225$), for which laminar stress-strain relation occurs, so that $y^* = U^*$. The quantities y^* and U^* are the dimensionless wall distance and dimensionless velocity respectively, defined as follows:

$$y^* = \frac{\rho C_\mu^{1/4} k_p^{1/2} y_p}{\mu} \quad (1)$$

$$U^* = \frac{U_p C_\mu^{1/4} k_p^{1/2}}{\tau_w / \rho} \quad (2)$$

where k_p is the turbulence kinetic energy at the near-wall node P , C_μ is an empirical constant equal to 0.09, y_p is the distance from point P to the wall, μ is the dynamic viscosity of the fluid, ρ is the density of the fluid, U_p is the mean velocity at node P and τ_w the wall shear stress.

In the log-law sub-layer ($y^* > 11.225$), logarithmic dependence between dimensionless velocity and wall unit occurs:

$$U^* = \frac{1}{\kappa} \ln(Ey^*) \quad (3)$$

where κ is the von Karman constant (equal to 0.4187) and E is an empirical constant, equal to 9.793. The logarithmic law for mean velocity is known to be valid for $30 < y^* < 300$.

The standard wall function approach requires that the first cell outside the walls is in the log-layer region ($y^* > 11.225$). The scalable wall-function approach prevents from the deterioration of the results in case of highly refined grid ($y^* < 11.225$), thus avoiding an erroneous modelling of the viscous sub-layer and buffer regions. In particular, a limiter in the y^* calculation is introduced in Equation (3), so that:

$$\tilde{y}^* = \text{MAX}(y^*, y_{\text{limit}}^*) \quad (4)$$

where $y_{\text{limit}}^* = 11.225$.

These wall functions produce consistent results for grids of arbitrary refinement. For grids which are coarser than $y^* > 11.225$, the scalable wall-function approach will provide identical results to the standard wall function one. In the present investigation, it was found that the use of the standard wall function approach, instead of the scalable wall function one, leads to errors in the prediction of the valve characteristic which can be of the order of 6% with respect to the experimental data, if the near-wall mesh cell size is not appropriate.

3.2.2. Dynamic mesh and UDF

A dynamic mesh was used to deal with the motion of the poppet; in particular, the surface of the poppet was defined as the moving zone with rigid body motion solution, while all the remaining inner surfaces of the valve were set as stationary zones. The smoothing, layering and remeshing functions embedded in ANSYS Fluent were used to prevent excessive mesh distortion and the occurrence of negative volumes of the cells during the poppet displacement. The remeshing was activated if the maximum cell skewness exceeded a threshold equal to 0.9. A UDF was written in C code and compiled in ANSYS Fluent, in order to calculate the axial rigid body motion of the poppet. This function was used to calculate the net axial force acting on the poppet at each time instant, taking into account the spring and the fluid forces. In the UDF it is necessary to set the spring stiffness, the initial spring preload, as well as the initial poppet opening position and the surfaces of the poppet on which the fluid force is calculated.

3.2.3. Fluid type and cavitation sub-model

Preliminary simulations were carried out using a single-phase incompressible fluid; however, it was verified that negative values of the absolute pressure (up to about -20 bar) occurred in some zones of the fluid domain (in particular, near to sharp edges with high fluid velocity gradients, as well as in recirculation vortexes). Negative absolute pressure values are unphysical, and may result in a wrong estimation of the forces exerted by the fluid on the poppet. Although it was verified that the influence of such negative pressure regions is little, for a more rigorous approach a two-phase mixture was chosen as working fluid, which is constituted by incompressible liquid phase (DTE25 oil at 40°C) and vapour phase, setting a constant vaporization pressure. The Schnerr and Sauer cavitation sub-model (Schnerr *et al.* 2001) embedded in ANSYS Fluent was used to estimate the expression of the net mass transfer from liquid to vapour. Obviously in the real valve the gaseous phase will be also constituted by separated air, however such aspect goes beyond the scope of the present paper.

3.2.4. Boundary conditions, discretization schemes and solution methods

For all simulations, a steady-state flow solution was preliminarily calculated and set as the initial condition for the time-dependent solution. The inlet mass flow rate at port P and the outlet pressure at port T were set as boundary conditions. The vapour mass fraction at the inlet and outlet of the valve was set to zero.

The pressure-based coupled algorithm was used to solve the momentum and pressure-based continuity equations together, so as to speed-up convergence.

The gradients were evaluated using the Green–Gauss node based method, which is usually recommended for tetrahedral meshes. The PRESTO! discretization scheme was used for the pressure equation, the QUICK one for

the momentum and volume fraction equations, and the first-order upwind one for the turbulent kinetic energy and turbulent dissipation rate equations. A relaxation factor of 0.3 was set for the volume fraction equation due to convergence issues in preliminary tests which were carried out using higher values of that coefficient. First order implicit formulation was used for the time marching in the transient simulations.

3.3. Model validation

3.3.1. Grid independence study

A grid independency study has been carried out in order to find the optimal mesh configuration.

In particular, the operating condition at 50 L/min and high spring preload has been considered as the most suitable one for this analysis, as it leads to the highest flow velocity distributions and to the highest values of the flow forces acting on the poppet and on the deflector. Figure 7 reports the effect of the number of cells of the grid on the calculated inlet pressure (Figure 7(a)) and on the calculated net force acting on the poppet, including the flow deflector (Figure 7(b)). The different mesh configurations were built by keeping the ratio between the dimension of the cells in the refinement zones constant.

It can be seen in the Figure 7 that a grid independent solution can be achieved using at least 2 million cells. This has been considered as the optimal mesh configuration for all the simulations (the selected configuration is highlighted with a red circle in the figure). The resulting computational time to simulate a single point of the flow-pressure characteristic resulted to be of the order of 3–4 h using 14 processes in parallel on an eight-core HT Xeon processor at 3.4 GHz.

3.3.2. Comparison between the predicted and experimental valve characteristics

The dynamic 3D-CFD model has been validated by carrying out a comparison between the experimental flow-pressure characteristics of the valve and the predicted ones. Figures 8–10 show the experimental and the simulated curves for three spring preload settings (low, medium, high) and for the three considered geometrical configurations of the flow deflector, i.e. geometry A, B and C.

It can be observed that the agreement in general is very good. The deflector resulted to be effective for the flow force compensation, especially for medium and high spring settings (for which the characteristic is vertical), while it is less effective for the low spring setting. This is due to the fact that, at a given flow rate, the poppet opening tends to reduce when the spring setting increases, so that the flow velocities in the metering edge and the axial momentum variation induced by the deflector increase. It can be observed that for geometry A (Figure 8) the flow-pressure characteristic for the high spring setting case tends to have a negative

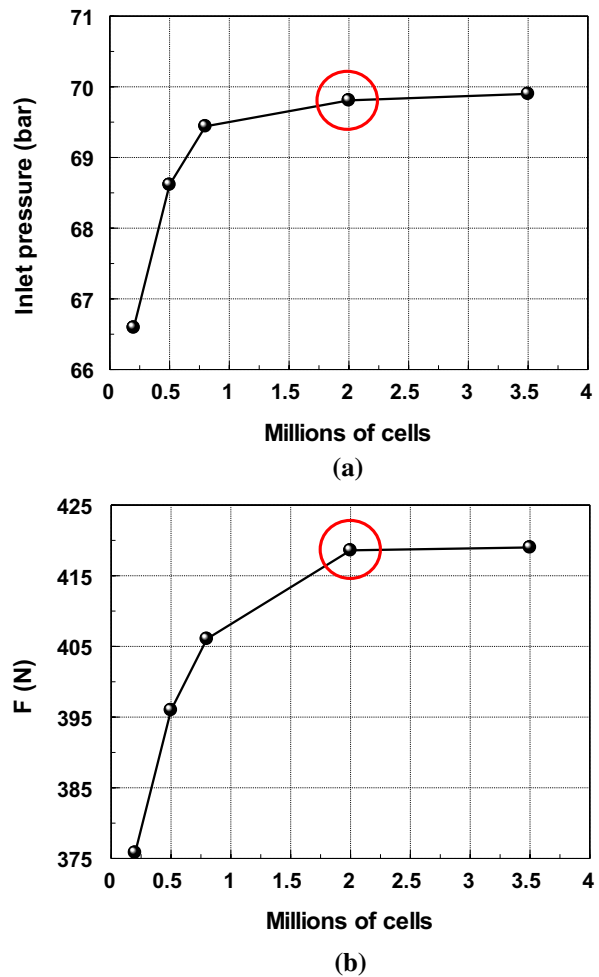


Figure 7. Effect of the number of cells on inlet pressure (a) and net poppet force (b).

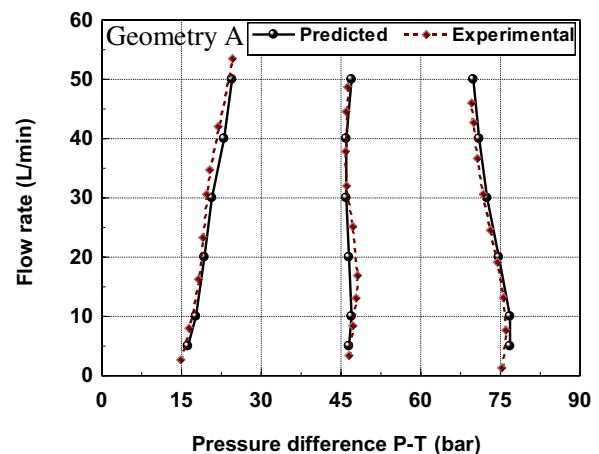


Figure 8. Predicted vs. experimental curves (geometry A).

slope at high flow rates, and this is due to an excessive flow force compensation. In general, a reduction in the depth of the deflector leads to a decrease in the slope of the flow-pressure characteristics, which can be observed especially for geometry C (see Figure 10).

It will be shown in the next section that this is due to a reduction in the variation of the flow axial momentum induced by the deflector.

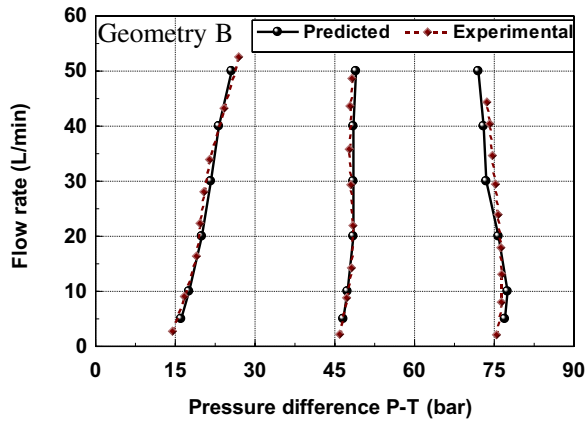


Figure 9. Predicted vs. experimental curves (geometry B).

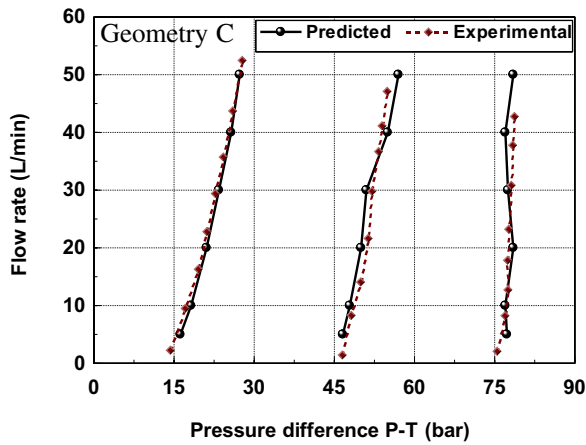


Figure 10. Predicted vs. experimental curves (geometry C).

3.4. Effects of spring setting

It was shown in the previous section that the deflector is effective for flow force compensation, especially for medium-high spring settings, while it is less effective at low spring settings. This can be explained on the basis of the results of the CFD simulations reported in Figures 11 and 12.

In particular Figure 11 reports, for the geometry A configuration, the velocity fields on the mid-plane of the valve which includes the axes of the inlet and outlet ports at 50 L/min and for the high and low spring settings, while Figure 12 reports the related pressure fields for the low, medium and high spring settings. For the sake of clarity only half poppet has been displayed, considered the symmetry of the geometry. Moreover, with reference to the pressure fields (Figure 12), only the zone in front of the deflector is shown.

In general, it can be observed in Figure 11 that a high flow deflection occurs; the estimated average angles of the fluid outflowing from the deflector are of the order of 170° for the high and medium spring settings, and of the order of 155° for the low spring setting.

It can also be observed in Figure 11 that the flow velocity in the metering edge tends to increase with the

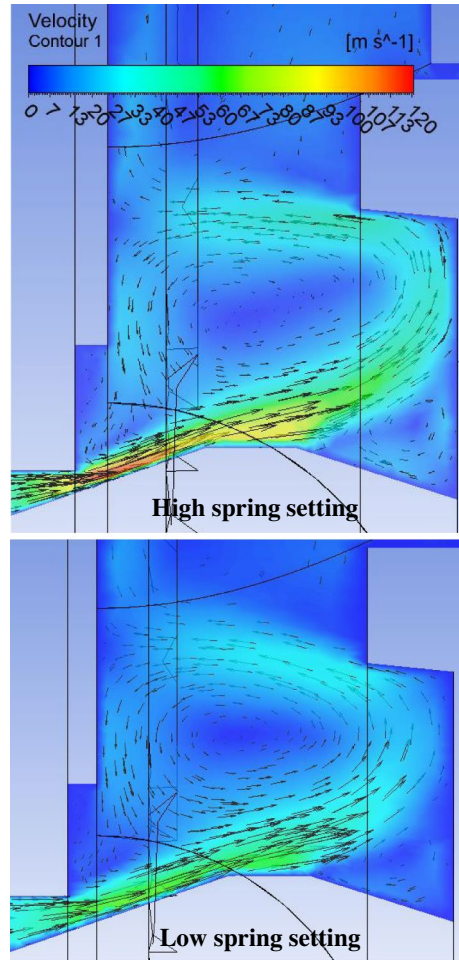


Figure 11. Velocity fields at 50 L/min and geometry A.

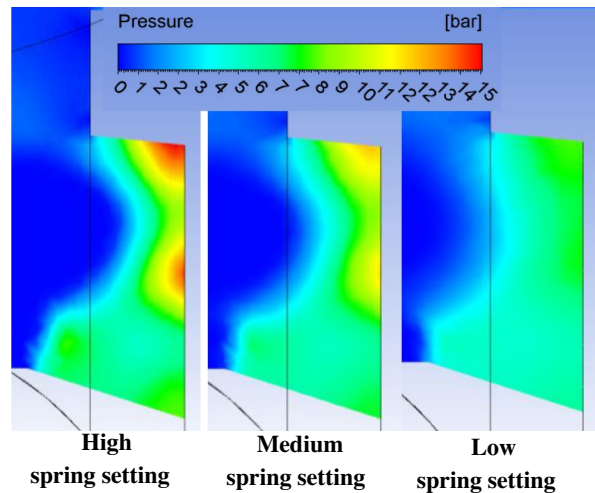


Figure 12. Pressure fields at 50 L/min and geometry A in the zone in front of the deflector.

spring setting, as a consequence of a decrease in the poppet opening position. Hence, also the velocity of the fluid which impacts the deflector tends to increase with the spring setting, and this determines a higher axial momentum variation induced by the deflector, even though the inlet and outlet flow angles are of the same order of magnitude for the three spring settings.

It can also be observed in Figure 11 that a recirculation of the fluid occurs in the volume downstream from the metering edge, especially for the high setting, and this generates an additional opening force contribution on the deflector. As a consequence, a higher pressure distribution on the flow deflector occurs when the spring setting increases, as can be seen in Figure 12, and this determines a higher flow force exerted by the fluid on the deflector.

For the same conditions, Figure 13 reports the fields of the vapour volume fraction. It can be observed that vapour formation occurs around the edges of the poppet, where the pressure tends to decrease to a great extent due to the high velocity gradients, and in the middle of the recirculation vortex. In general, the higher volume fractions occur for high spring settings, due to the higher flow velocities which determine higher pressure drops.

3.5. Effects of deflector geometry

Figures 14 and 15 report the velocity fields at 50 L/min for the configurations A and C of the flow deflector with the high and low spring settings respectively.

It can be seen in the figures that, at both low and high spring settings, a reduction in the depth of the deflector leads to a decrease in the angle of the fluid outflowing from the deflector; moreover, the recirculation of the fluid is also reduced to a great extent. Both effects contribute to a reduction in the flow force compensation of the flow deflector.

3.6. Effect of the poppet cone angle

An investigation of the effect of the poppet cone angle has been carried out. In particular, a variation of ± 5 deg with respect to the baseline geometrical configuration (i.e. 19.2°) has been analysed. The condition at 50 L/min and high spring setting has been selected for the comparison, as it leads to the highest flow forces acting on the poppet and on the deflector, and is therefore the most suitable one for the evaluation of the effects of geometrical variations of the valve on the flow forces. The results of the simulations for this operating point are visible in Figures 16 and 17, in terms of velocity and pressure fields, respectively.

In order to better analyse the results, Table 2 reports the effect of the poppet cone angle on the inlet pressure, poppet opening position and the force F_{def} acting on the flow deflector.

First, it can be noted in Figure 16 that an increase in the poppet cone angle leads to a different impact point of the flow on the deflector.

It can be seen in Table 2 that an increase in the poppet cone angle leads to a reduction in the poppet opening position: this is a geometrical effect, and is due to the fact that if the cone angle increases, a lower poppet opening position is sufficient to achieve the same cross-sectional

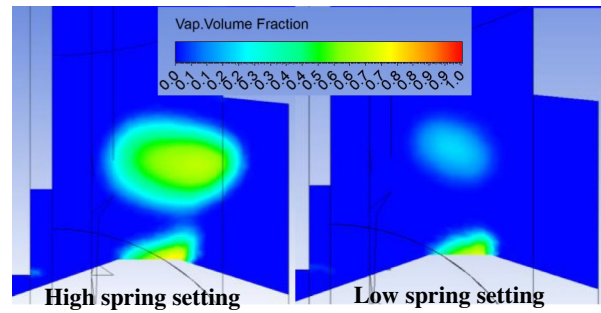


Figure 13. Vapour volume fraction fields at 50 L/min and Geometry A.

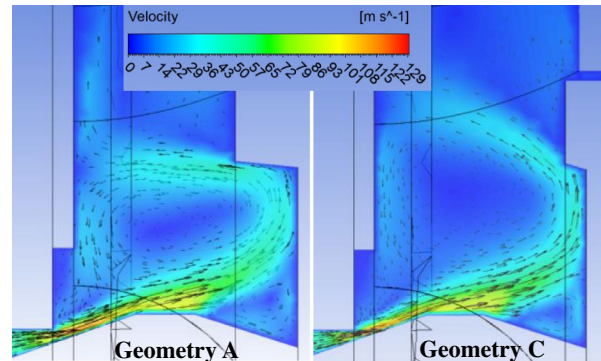


Figure 14. Velocity fields at 50 L/min, geometries A and C, high spring setting.

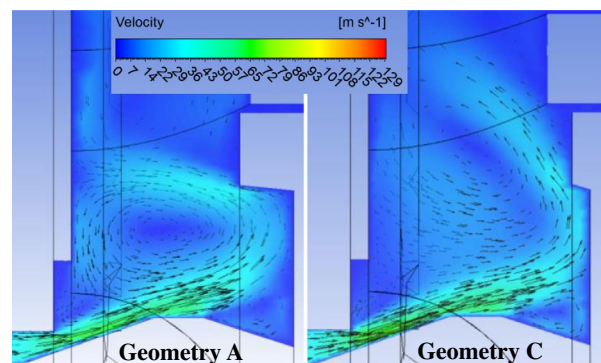


Figure 15. Velocity fields at 50 L/min, geometries A and C, low spring setting.

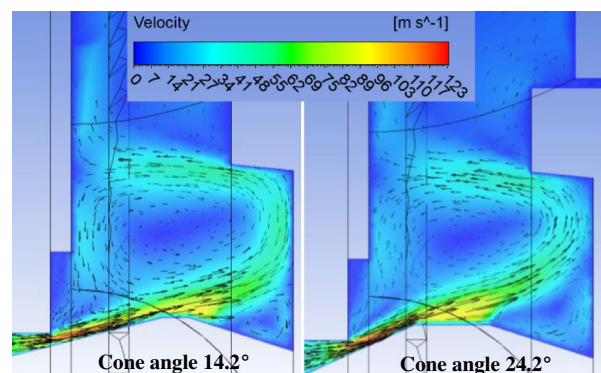
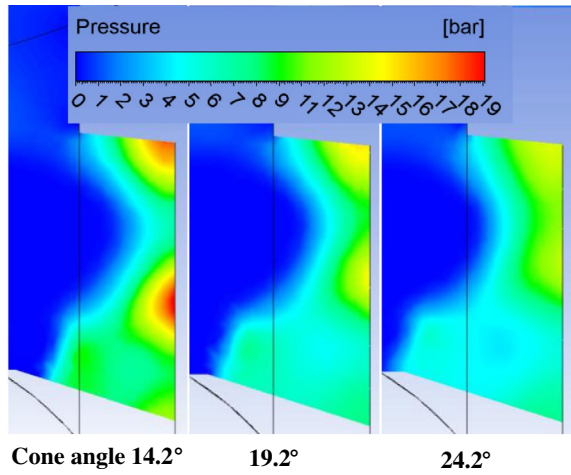


Figure 16. Velocity fields, at 50 L/min, different poppet angles, high spring setting.

Table 2. Effect of cone angle at 50 L/min and high setting.

Cone angle	Inlet pressure (bar)	Poppet position (mm)	Deflector force (N)
14.2°	72.5	1.29	205
19.2° (baseline)	69.8	1.02	195
24.2°	73.6	0.82	179

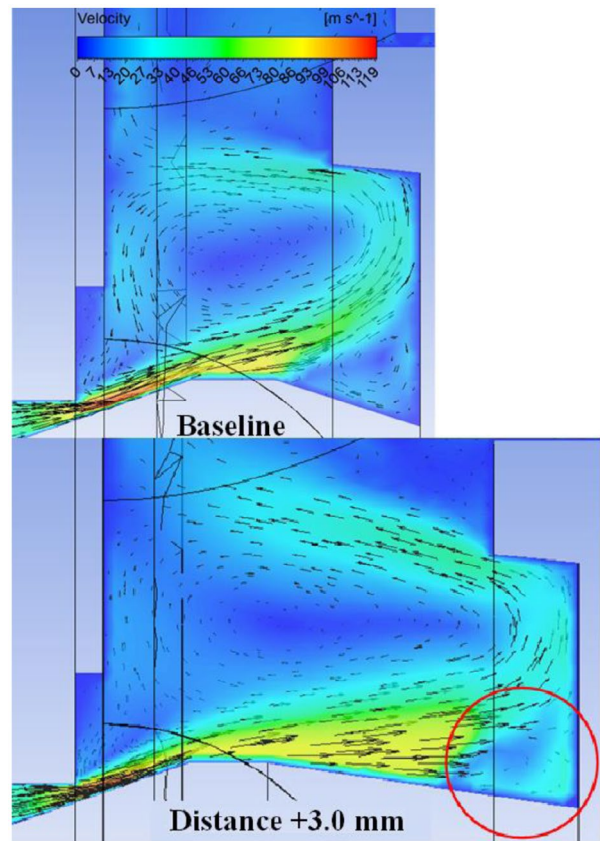
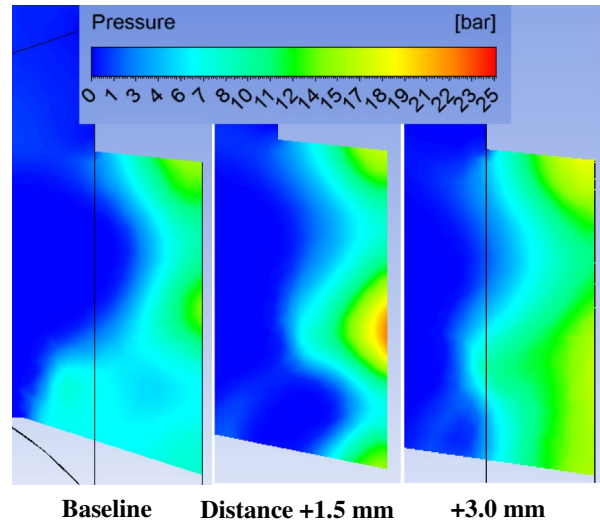
**Figure 17.** Pressure fields, at 50 L/min, different poppet angles, high spring setting.

area in the metering edge. This would lead to a benefit in terms of the valve characteristic (i.e. to a reduction in the inlet pressure at equal flow rate), because a lower spring compression is necessary to achieve the same cross-sectional area. However, it can be seen in Table 2 that an increase in the poppet cone angle also leads to a decrease in the flow force acting on the flow deflector, which has instead a negative effect on the valve characteristic. This can also be observed in Figure 17, where it can be seen that lower pressure distributions occur on the flow deflector at increasing cone angles, as a consequence of a different angle of the flow impacting the deflector and of the fluid outflowing from it.

As a result, the net effect of a variation in the poppet cone angle on the valve characteristic depends on which of the two effects is predominant. For the analysed conditions, both a reduction and an increase in the poppet cone angle of 5 deg lead to a detriment in the valve characteristic (i.e. to an increase in the inlet pressure at fixed flow rate), so that the baseline geometrical configuration can be considered as the optimal one.

3.7. Effect of deflector distance

An investigation of the effect of the deflector distance from the poppet seat has also been carried out. In particular, variations of +1.5 mm and of +3.0 mm, with respect to the baseline geometrical configuration, have been analysed. As in the previous case, the condition at 50 L/min and high spring setting has been selected for the comparison; the velocity and pressure fields are shown in Figures 18 and 19, respectively.

**Figure 18.** Velocity fields, at 50 L/min, different deflector positions, high spring setting.**Figure 19.** Pressure fields, at 50 L/min, different deflector positions, high spring setting.

In order to better analyse the results, Table 3 reports the effect of the deflector distance at 50 L/min on the inlet pressure, poppet opening position and flow force acting on the flow deflector.

It can be seen that an increase in the distance has little influence on the values of the inlet pressure and of the flow forces. This can also be clarified by analysing the velocity fields reported in Figure 18: although a spreading of the jet occurs when the distance of the flow

Table 3. Effect of deflector distance at and high setting.

Distance from poppet seat	Inlet pressure (bar)	Poppet position (mm)	Deflector force (N)
Baseline	69.8	1.02	195
+1.5 mm	69.0	1.02	200
+3.0 mm	69.9	1.02	190

deflector increases, and the angle of the fluid outflowing from the deflector tends to decrease (both effects would negatively affect the performance of the deflector), it can be seen that a small recirculation zone of fluid arises in the central portion of the deflector (which is highlighted by a red circle in the figure), which gives a positive contribution on the fluid force acting on the deflector, as can also be seen from the pressure fields in Figure 19. As a result, the net flow force acting on the deflector is almost independent on the position of the deflector.

4. Lumped parameter model

4.1. Model description

As just demonstrated, the presented CFD model is able to predict with a good accuracy the steady-state characteristic. However the 3D approach cannot be used in a study of a whole system, where the pressure relief valve represents only one of the numerous components. In such a case, a lumped parameter model is the only valid alternative. As a consequence a simplified analytical expression for the forces F_{jet} and F_{def} (see Figure 2) must be determined. At steady-state conditions, the flow force F_{jet} can be evaluated using the well-known equation, function of the flow rate Q and the fluid velocity v , which derives from the fluid axial momentum conservation:

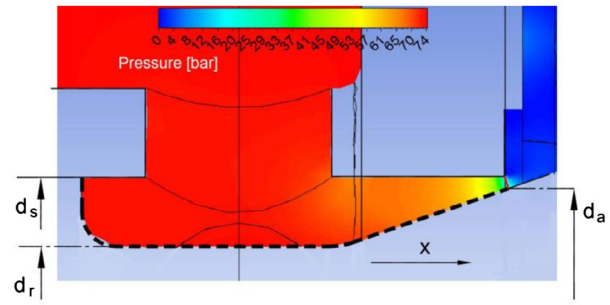
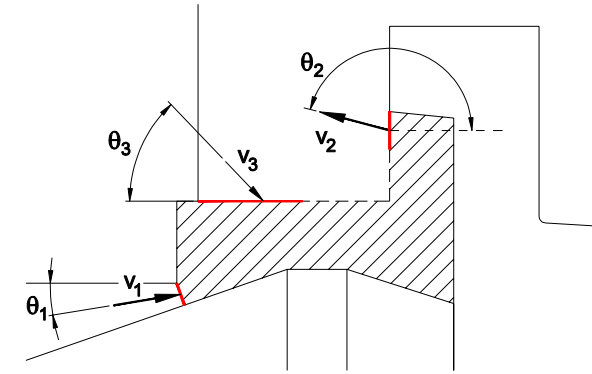
$$F_{jet} = \rho Q v \cos \alpha \quad (5)$$

In this case the jet angle can be approximated with the poppet half-angle α . The flow force calculated with Equation (5) at 50 L/min and opening x of 1 mm is 88.2 N, against a value obtained by the CFD model of 85.1 N.

The latter value was calculated as the resultant along the x axis of the pressure distribution acting on the dashed line in Figure 20. In particular the flow force is the difference between two contributions: the term acting on the surface of the dumper from the rod diameter d_r up to the seat diameter d_s , and the force due to the pressure acting on the cone from d_r up to the diameter d_a identifying the minimum area.

For the evaluation of the force on the flow deflector, it is possible to apply the conservation of the fluid momentum on the hatched volume in Figure 21.

In fact the flow enters the control volume through the restricted flow area and, as shown in the CFD simulations (see Figure 11), it leaves the flow deflector in correspondence of the outer edge with a velocity v_2 . If the angle θ_2 is close to 180° , then the jet hits the seat of

**Figure 20.** Pressure at 50 L/min, high setting, geometry A.**Figure 21.** Control volume.

the poppet and a fraction of the outgoing fluid is recirculated. In such case a second inlet flow area must be considered with a fluid velocity v_3 and an angle θ_3 .

Hence the force on the flow deflector is:

$$F_{def} = \rho Q (v_1 \cos \theta_1 - v_2 \cos \theta_2 + v_3 \cos \theta_3) \quad (6)$$

The velocity v_1 in the vena contracta can be written as function of the flow rate and of the flow area. Moreover the fluid jet enters the control volume with an angle that depends on the cone angle; in particular θ_1 can be assumed as the average between the half angle of the poppet α and the angle of the seat (0°). Therefore Equation (6) can be rearranged as follows:

$$F_{def} = \frac{\rho Q^2}{C_d A} \left(\cos \left(\frac{\alpha}{2} \right) - k_{21} \cos \theta_2 + k_{31} \cos \theta_3 \right) \quad (7)$$

where the coefficients k_{21} and k_{31} represent the ratio between the maximum fluid velocity in the sections 2 and 3 respectively and the velocity in the inlet section 1.

Finally the opening force F_{act} due to the inlet pressure is simply expressed as:

$$F_{act} = \frac{d_s^2 \pi}{4} p_{in} \quad (8)$$

A lumped parameter model of the valve was developed in the LMS Imagine.Lab AmesimTM environment. In Figure 22 the model of the valve built with the Hydraulic

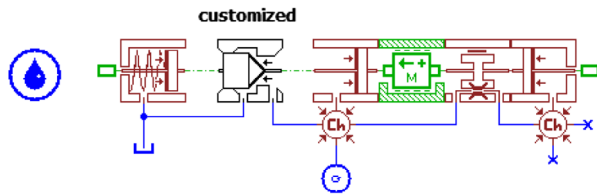


Figure 22. LMS Amesim model of the valve.

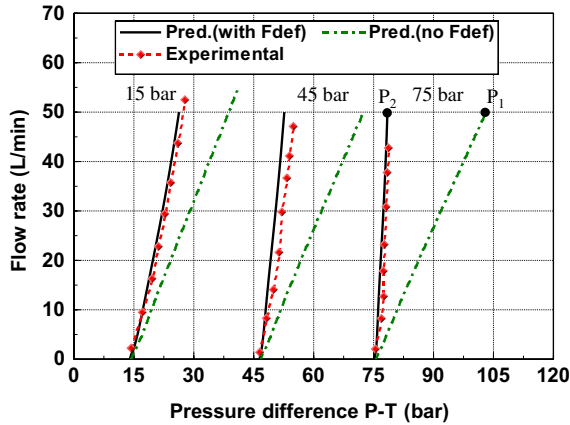


Figure 23. Predicted vs. experimental curves, Geometry C.

Component Design library is reported (Amesim User's Guide, 2015) and the customized component implementing the expression (11) is highlighted.

A flow source is connected to the inlet port, while the spring chamber is connected directly with the tank.

4.2. Model performance

The comparison between the experimental points and the simulated characteristics is reported in Figure 23 for three different pressure settings and Geometry C. In such a case, based on the CFD simulations, the recirculation is negligible and, accordingly, the term k_{31} has been set to 0. The simulations have been performed with $\theta_2 = 120^\circ$ and $k_{21} = 0.4$; both values come from the CFD simulation at 50 L/min and maximum pressure setting (see Figure 14). In the same figure the curves simulated without the force F_{def} are also superimposed (no F_{def}), allowing to appreciate the significant contribution of the force induced by the deflector. In fact at the maximum pressure setting and maximum flow rate, the deflector allows to reduce the real regulated pressure from 103 bar (point P_1) to 78.5 bar (point P_2). In this operating point the force F_{def} calculated with the Equation (7) is equal to 116 N.

With the Geometry A (Figure 24), in the same operating point the experimental final regulated pressure is about 69 bar and the force F_{def} can be estimated to be about 159 N. If the recirculation is not taken into account (no recirc.), the simulated deflector force is 132 N (point P_3) with an error of 17%, using $\theta_2 = 170^\circ$, based on Figure 11.

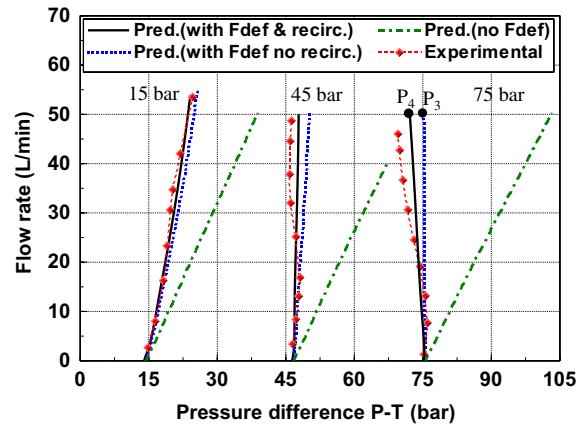


Figure 24. Predicted vs. experimental curves, Geometry A.

However the CFD simulations show that a fraction of the flow rate is recirculated and the coefficient k_{31} is about 0.25. The angle θ_3 is not easy to be determined, so a value of 45° can be a good compromise. In this case P_4 becomes the new final point and the force is 146 N with an error of 8%. It should, however, be noted that such value represents the maximum error, since for lower flow rates or lower pressures the simulated curves are closer to the experimental data.

5. Conclusion

In this paper two modelling approaches for assessing the steady-state characteristic of a flow force compensated pressure relief valve are presented. A 3D CFD model with interaction between the pressure field and the poppet position has been developed in ANSYS Fluent. It has been demonstrated that such model can be used as a fully predictive tool for the evaluation of the valve behaviour, since it does not require any tuning on experimental tests. It was verified that, in order to obtain physically consistent results, a cavitation model has to be adopted, and particular attention must be paid to the choice of the correct wall function approach.

Moreover a very good agreement between the predicted and measured curves was found. The model was also proved to be reliable in evaluating the effect of a geometrical modification of the flow deflector.

A significant outcome from the study is that the flow force compensation is mainly affected by the depth of the deflector, while the cone angle and the deflector distance have a negligible effect. The lumped parameter model requires a tuning on CFD data, however reasonably good results can be obtained with just one CFD steady-state simulation performed in the condition of maximum flow rate and maximum pressure setting. Since the presented CFD model takes into account also the dynamics of the valve, it can reasonably be used to investigate transient phenomena.

Nomenclature

Symbols

A	minimum flow area
C_d	discharge coefficient
C_μ	constant in Equations (1) and (2)
d_a	diameter for minimum flow area
d_r	rod diameter
d_s	seat diameter
E	constant in Equation (3)
F_{act}	opening force
F_{def}	force on the flow deflector
F_{jet}	flow force on the conical poppet
F_{spr}	spring force
k_{31}	velocity ratio v_3/v_1
k_{32}	velocity ratio v_3/v_2
k_p	turbulence kinetic energy
p_{in}	inlet pressure
Q	volumetric flow rate
U_p	mean velocity at node P
U^*	dimensionless velocity
V	fluid velocity
y_p	distance of point from the wall
y^*	dimensionless wall distance
α	poppet half angle
θ	jet angle
κ	von Karman constant
τ_w	wall shear stress
μ	dynamic viscosity of the fluid
ρ	fluid density

Acronyms

PRESTO	PREssure STaggering Option
QUICK	Quadratic Upwind Interpolation for Convective Kinetics
RANS	Reynolds Averaged Navier-Stokes

Disclosure statement

No potential conflict of interest was reported by the authors.

Notes on contributors



Roberto Finesso graduated 'magna cum laude' in Mechanical Engineering at the Politecnico di Torino in 2005. He took a PhD in Energy Engineering, section 'Fluid Flow Machines', at the Energy Department at the Politecnico di Torino in 2009, and he has worked as post-doc fellow from 2009 to 2012. In 2012 he joined the Faculty as Assistant Professor with a time-contract position. His research activities are mainly focused on CFD modelling of fluid power components, especially valves, and on combustion and emission formation modelling in internal combustion engines.



Massimo Rundo graduated in Mechanical Engineering at the Politecnico di Torino in 1996. After graduation he participated with the Fluid Power Group of the Politecnico di Torino, as a visiting researcher, to an extensive research project on lubrication pumps for internal combustion engines. In 2005 he joined the Faculty as Assistant Professor. He is lecturer of Fluid Power courses from 2006. His research activity is mainly focused on modelling, simulation and testing of fluid power components, especially positive displacement pumps.

ORCID

Roberto Finesso  <http://orcid.org/0000-0002-9327-2237>
 Massimo Rundo  <http://orcid.org/0000-0001-6868-6174>

References

- Andersen, T.O., Hansen, M.R., Sørensen, H.L., 2003. Using CFD to establish a correlation between design parameters and performance characteristics for seat valves. *In: Proceedings of 1st intl conference on computational methods in fluid power technology – methods for solving practical problems in design and control*, Melbourne, Australia.
- Ansys, Inc., 2011. *Ansys FLUENT 14 theory guide*.
- Bernad, S.I. and Resiga, R.S., 2012. Numerical model for cavitation flow in hydraulic poppet valves. *Modelling and simulation in engineering*, 2012. Article ID: 742162, 10 pages. doi:10.1155/2012/742162.
- Del Vescovo, G., Lippolis, A., 2003. CFD analysis of flow forces on spool valves. *In: Proceedings of the 1st international conference on computational method in fluid power technology*, Melbourne, Australia.
- Domagala, M., Lisowski, E., 2004. Determination of flow forces in hydraulic valves. *In: Proceedings of the 3rd FPNI – PhD symposium on fluid power*, Terrassa, Spain.
- Domagala, M., Lisowski, E., 2003. Determination of relief valve characteristics by the use of CAD system and CFD tools. *In: Proceedings of the 1st international conference on computational method in fluid power technology*, Melbourne, Australia.
- Gao, H., Fu, X., Yang, H., 2002. Numerical investigation of cavitating flow behind the cone of a poppet valve in water hydraulic system. *Journal of Zhejiang university science*, 3 (4), 395–400.
- Huguet, D., 2003. CFD analysis of flow forces on direct acting relief minivalves. *In: Proceedings of the 1st international conference on computational method in fluid power technology – SIM2003*, Melbourne, Australia.
- Huguet, D., 2004. Dynamic mesh modelling of a direct acting relief valve. *In: Proceedings of the 3rd FPNI – PhD symposium on fluid power*, Terrassa, Spain.
- Jalil, J., Ahmed, S., Xue, Y. and Ghadband, S., 2015. Experimental and numerical investigation of fluid flow of truncated conical poppet valve. *International journal of fluid power*, 16 (1), 25–34. doi:10.1080/14399776.2015.1017360.
- Lauder, B.E. and Spalding, D.B., 1974. The numerical computation of turbulent flows. *Computer methods in applied mechanics and engineering*, 3, 269–289.
- Schnerr, G.H., and Sauer, J., 2001. Physical and numerical modeling of unsteady cavitation dynamics. *In: Fourth international conference on multiphase flow*, New Orleans, USA.

- Siemens PLM Software, 2015. *LMS Imagine.Lab Amesim – hydraulic component design library 14, user's guide*
- Vaughan, N.D., Johnston, D.N., and Edge, K.A., 1991. Experimental investigation of flow and force characteristics of hydraulic poppet and disc valves. *Proceedings of the institution of mechanical engineers, part a: journal of power and energy*, 205 (3), 161–171, doi:10.1243/PIME_PROC_1991_205_025_02.
- Vaughan, N.D., Johnston, D.N., and Edge, K.A., 1992. Numerical simulation of fluid flow in poppet valves. *Proceedings of the institution of mechanical engineers part c journal of mechanical engineering science*, 206 (2), 119–127. doi:10.1243/PIME_PROC_1992_206_105_02.